A multi-objective optimal design method for thermal energy storage systems with PCM: a case study for outdoor swimming pool heating application

Yantong Li[a,b,*] Zhixiong Ding[c], Mohammad Shakerin[b], Nan Zhang[a]

[a]Department of Architecture and Civil Engineering, City University of Hong Kong, Tat Chee Avenue, Kowloon, Hong Kong, China

[b]Department of Energy and Process Technology, Norwegian University of Science and Technology, Kolbjørn Hejes vei 1 B, Trondheim 7491, Norway

[c]School of Energy and Environment, City University of Hong Kong, Tat Chee Avenue, Kowloon, Hong Kong, China

*Corresponding author; Tele: 852-56100432; 86-14714316174; Email: yantong.li@ntnu.no

ABSTRACT

Traditional design methods for thermal energy storage systems (TES) with phase change material (PCM) are mostly based on worst-case scenario, which causes too large size of main components. Current optimal design methods for these systems mainly focus on single optimization objective, which only satisfies the unilateral requirement. A multi-objective optimal design method for these systems is urgently needed, and therefore this paper remedies this knowledge gap. The response surface methodology is adopted to develop the surrogated models of the optimization objectives to improve the computational efficiency. Then, the non-dominated sorting genetic algorithm II is used to perform the double-objective and triple-objective optimization for acquiring the Pareto optimal solutions. Finally, the final decision-making methods that includes LINMAP and TOPSIS are adopted to identify the final optimal solutions. A case study of optimizing the design for an outdoor swimming pool (OSP) heating system with PCM storage tank, is conducted to illustrate the proposed approach. Eight final optimal solutions were identified, and the s_p of the system in these solutions was 1.05, 1.24, 1.04, 1.22, 1.06, 1.06, 1.07, and 0.88 years, respectively. Results indicate that the proposed approach is effective to conduct the multi-objective optimization for the OSP heating systems and guide the design optimization for the TES systems with PCM.

Keywords: Multi-objective optimization; Thermal energy storage; Phase change material; Outdoor swimming pool; Heating system

Nomenclature

Abbreviations		F_{rs}	r_{th} value for the s_{th} objective
AHP	Air-source heat pump	$F_{s}^{non-ideal}$	non-ideal value for the s_{th} objective
AOVA	analysis of variance	F_{s}^{ideal}	ideal value for the s_{th} objective
CCD	central composite design	fd	off-peak period
DOE	design of experiment	G_p	p_{th} equality constraint
DOSE	design of simulated experiments	H_{pcm}	enthalpy of PCM
FDM	final decision-making	H_{pm}	latent heat of PCM
MOO	multi-objective optimization	H_q	q_{th} inequality constraint
NSGA-II	non-dominated sorting genetic algorithm II	k_{wt}	thermal conductivity of water
OSP	outdoor swimming pool	L	number of decision parameters
PCM	phase change material	M	number of objective functions
PST	PCM storage tank	m_d	designed water flow rate
RSM	response surface methodology	m_p	water flow rate
		n	number of experimental samples
Symbols		od	on-peak period
a_c	rate for the discount in the market	o_r	operating cost saving ratio
c_{iap}	initial cost of AHPs	P	number of equalities
c_{icr}	initial cost of controllers	p_d	designed power of pumps
c_{ihe}	initial cost of heat exchangers	Q	number of inequality constraints
c_{ip}	initial cost of pumps	q_a	heating capacity of AHPs
c_{ipt}	initial cost of PST	q_{pl}	total heat flux of OSP
c_{it}	initial expense of the system	R	number of the Pareto optimal solutions
c_{itc}	initial cost of thermal-insulation cover	r_c	rate for the increase of the electricity

c_{iv}	intercept value	s_p	simple payback period
c_k	coefficient of the linear items	T_{dpl}	designed water temperature of OSP
c_l	lifecycle expense	$T_{ex,j}$	experimental temperature values
c_{lp}	liquid specific heat of PCM	T_{pcm}	temperature of PCM
c_{ot}	operating expense of the system	T_{pl}	temperature of OSP
c_{o1}	operating expense in the first year of the lifecyle	T_{pm}	melting temperature of PCM
c_{rl}	lifecycle expense generated by simulation platform	T_{pt}	designed maximum temperature that AHPs can heat up to
c_{rn}	coefficient of the interaction items	$T_{si,j}$	simulated temperature values
c_{rr}	coefficient of the quadratic items	t	time
c_{sp}	solid specific heat of PCM	t_{cp}	thermal comfort unmet time percentage
c_{ut}	an indicator applied to assess whether the thermal comfort requirement is satisfied	t_{ot}	total time when OSP is open in winter season
D	design variable	t_{rcp}	thermal comfort unmet time percentage generated by simulation platform
DE_{r+}	Euclidian distance between each Pareto optimal and the ideal solution	u_{wt}	mean velocity of water
DE_{r-}	Euclidian distance between each Pareto optimal and the non-ideal solution	V_{mp}	maximum volume of PST
dc	cost caused by the demand charge	V_p	volume of PST
E_{st}	maximum required thermal energy of OSP during the open period for satisfying thermal comfort requirements	V_{pl}	volume of OSP

ec	the cost caused by the energy charge	X	response objective
e_{ai}	energy use of AHPs	x	distance
e_i	energy use of the system in the i^{th} year within the lifetime of the year	$\boldsymbol{z}$	vector of decision parameters
e_{pi}	energy use of pumps		
e_r	energy saving ratio	*Greek symbols*	
e_{rr}	random error	Δ_{ts}	a user-defined threshold
e_{rt}	total energy use generated by simulation platform	ε_{ae}	average relative error
e_t	total energy use	ε_{wt}	water fraction
F_m	m_{th} objective function	ρ_{pcm}	density of PCM

1. Introduction

Increasing population and environmental pollution promote the use of renewable energy [1, 2]. Thermal energy storage (TES) plays a lot of significant roles in the renewable energy utilization, including overcoming the intermittency of solar energy in heating systems [3, 4], and enhancing the utilization efficiency of cold air energy in free cooling systems [5, 6]. The merits of phase change material (PCM) that includes low capital cost and high energy storage density, enable it very popular in the TES in comparison with sensible and thermochemical storage material [7-10]. Therefore, TES with PCM is applied in a variety of systems, such as passive cooling system [11], concentrated solar power system [12], direct steam generation system [13], solar still system [14], and batteries thermal management system [15].

Various studies have been conducted in the TES systems with PCM. Some scholars analyzed the thermal performance of the TES systems with PCM. For instance, Korti and Tlemsani [16] analyzed the influence of water inlet temperature, water mass flow rate, and types of PCM on the charging and discharging completion time. It was concluded that the effect of water mass flow rate on charging process was greater than that on discharging process. Siyabi et al. [17] experimentally and numerically analyzed the melting performance of a cylindrical PCM storage unit, and found that the melting profile of the PCM was not affected by the charging rate. Some scholars performed the energy analysis of the TES systems with PCM. For instance, Hasan at al. [18] compared the energy performance of the photovoltaic system with and without PCM. It was found that the annual electricity yield in hot climates was increased by 5.9% when the PCM was used. Senthil and Cheralathan [19] found that the energy efficiency of the solar receiver with multiple PCM storage units could reach 66.7%. In addition, some scholars estimated the economic performance of the TES systems with PCM. For instance, Maatallah et al. [20] reported that the payback period of a photovoltaic system with PCM was nearly 6 years. Chaiyat [21] found that the payback period of a building air-conditioner was approximately 4.5 years.

Optimal design is another research hotspot in the TES systems with PCM. For example, Arıcı et al. [22] identified the optimal PCM location, layer thickness, and melting temperature for maximizing the utilization of PCM latent heat in external walls of buildings. Pereira and Aelenei [23] conducted the optimal design of a building integrated photovoltaic system with PCM. The optimal PCM layer thickness, PCM latent heat, air flow rate, and air cavity thickness were determined for maximizing the energy performance of the system. Haillot et al. [24] presented the optimal design of a solar domestic hot water system with PCM for minimizing the energy consumption of the system. The optimal volume of PCM storage tank (PST) and PCM melting temperature were identified. However, most of current studies of the TES systems with PCM focus on realizing only one optimization objective.

In the traditional optimal design problem, only one optimization objective is considered for satisfying the requirement from single aspect [25-27]. However, in practical situations multiple optimization objectives should be carried out from different aspects [28-32]. For example, in the optimization of the integrated district cooling and heating systems, both minimizing the total cost and minimizing the CO_2 emissions were selected as the optimization objectives [33]. In the optimization of the solar-driven trigeneration system, maximizing the energy efficiency, maximizing the exergy efficiency, and maximizing the energy saving cash flow were considered as the optimization objectives [34]. In the optimization of the solar combi-systems, minimizing the lifecycle cost, minimizing the lifecycle energy use and minimizing the lifecycle exergy destroyed were selected as the optimization objectives [35]. In the optimization of the power generation system, minimizing the total expense, minimizing the CO_2 emission, and minimizing the probability of loss of power supply were considered as the optimization objectives [36]. Multi-objective optimal design methods have been proposed in many systems. However, a multi-objective optimal design method for the TES systems with PCM is still lacking.

To remedy this knowledge gap, this study therefore proposes a multi-objective optimal design method for the TES systems with PCM. This method will overcome the disadvantage of large computational load for simulating the complex heat transfer problem in the TES systems with PCM. Response surface methodology (RSM) will be adopted to develop the surrogated models of the TES systems according to the design combinations of the design variables and optimization objectives that are formulated by professional statistical and mathematical methods [37]. The non-dominated sorting genetic algorithm II (NSGA-II) [38] is adopted to conduct the multi-objective optimization (MOO) that is based on the developed surrogated models. The final decision-making (FDM) methods [39] are adopted to identify the final optimal solution from the Pareto optimal solutions.

To illustrate the proposed multi-objective optimal design method, a case study of outdoor swimming pool (OSP) heating application with PST is presented in this study. Swimming outdoor that allows people to enjoy the scenery while exercising, is the favorite activity for residences in subtropical climate cities such as Shenzhen and Hong Kong. Due to the warm ambient temperature in summer, the thermal comfort requirement of the OSP water temperature is easy to be satisfied without extra heat supply. Whereas, the ambient temperature reduces in winter, resulting in the heavy heat energy demand for meeting the thermal comfort requirement. Traditional heating techniques like electrical or gas boilers have the flaw of high operating cost when they are adopted to deal with this issue. Thus, most of OSPs are discontinued in winter, leading to the waste of the spaces and facilities.

To extend the available time of the OSPs in winter, a variety of heating technologies have been adopted to supply heat for the OSPs, like solar collectors [40, 41] and biomass heaters [42]. One heating technology is using air-source heat pumps (AHPs) that collects heat from the ambient air. For instance, Lam et al. [43, 44] utilized the AHPs to heat an OSP of a four-star hotel in Hong Kong. They concluded that the energy cost of the system with a COP of 3.5 could be reduced by $35,841 over a ten-years life cycle in comparison with a traditional heating system.

To enhance the economic performance of the system, AHPs are usually adopted together with thermal energy storage technologies. One commonly used approach is that the AHPs are adopted to store heat into the thermal energy storage units during the electric off-peak period, and the stored heat will be released for satisfying the heat demand during the electric on-peak period [45]. This contributes to two merits: one is that the selected heating capacity of the

AHPs during the design process can be reduced because it is not sized according to the peak heating load; and another is that the operating cost of the system will be reduced because the electric price during the off-peak period is lower than that during the on-peak period. However, the method that integrates the AHPs with thermal energy storage technology is few adopted in the OSP heating system. Hence, Li et al. [46, 47] carried out an OSP heating system with the combination of the AHPs and the PST. They reported that the proposed OSP heating system was viable from both economic and technical aspects. However, the optimal design of this system from multiple aspects is urgently needed for obtaining better performance of the system. Hence, this system is considered as a case study for illustrating the proposed multi-objective optimal design method for the TES systems with PCM.

The novelty of this study is presented as follows: (1) an optimal design method is proposed to fill the knowledge gap in the field of multi-objective optimal design for thermal energy storage systems with PCM; (2) system surrogated models are developed by RSM, contributing to improve computational efficiency; (3) double-objective and triple-objective optimization are obtained by NSGA-II, which results in Pareto optimal solutions; (4) final decision-making is conducted by LINMAP and TOPSIS, which can effectively determine final optimal solutions from Pareto sets; (5) the case study of a heating system for OSP applications demonstrate the applicability of the proposed method, which indicates that the proposed method can well guide the optimal design of thermal energy storage systems with multiple optimization objectives.

The rest of the paper is organized as follows: the proposed multi-objective optimal design methodology is introduced in Section 2. Section 3 presents the case studies. Section 4 depicts the results and discussion. Conclusions are given in Section 5.

2. Methodology

The comparison between the proposed multi-objective optimal design method and traditional design method for thermal energy storage systems with PCM is depicted in Fig. 1. In the traditional design method, the worst-case scenario is usually used to calculate the maximum heating or cooling power and energy demand. These values will be directly adopted to size the capacity of heating or cooling devices and volume of PCM storage devices. However, these values just represent the maximum sizes of heating or cooling devices and PCM storage devices. It will cause the waste of source if these devices with too big size are used in practical situations.

In the proposed multi-objective optimal design method, the worst-case scenario will be used to calculate the maximum and minimum heating or cooling demand. These values will be adopted to obtain the ranges of the capacity of heating or cooling devices, and volume of PCM storage devices. Based on these ranges, design of experiments methods will be adopted to make the schedule of simulated experiments. Typical cases for the combinations of design variables will be acquired. To obtain the values of the response objectives in these cases, the design variables should be input into the established complex simulation platform that consists of weather conditions, mathematical models, auxiliary devices, and operating strategies of the system. The RSM will be used to develop the multi-objective models according to the completed design cases. Then, the MOO will be performed adopting the developed multi-objective models and optimization methods. The Pareto optimal solutions including the combinations of optimal design variables and objectives will be acquired. The FDM for identifying the final optimal solution from the Pareto optimal solutions will be conducted using typical mathematical FDM approaches. Finally, the optimal capacity of heating or cooling devices and volume of PCM storage devices will be identified.

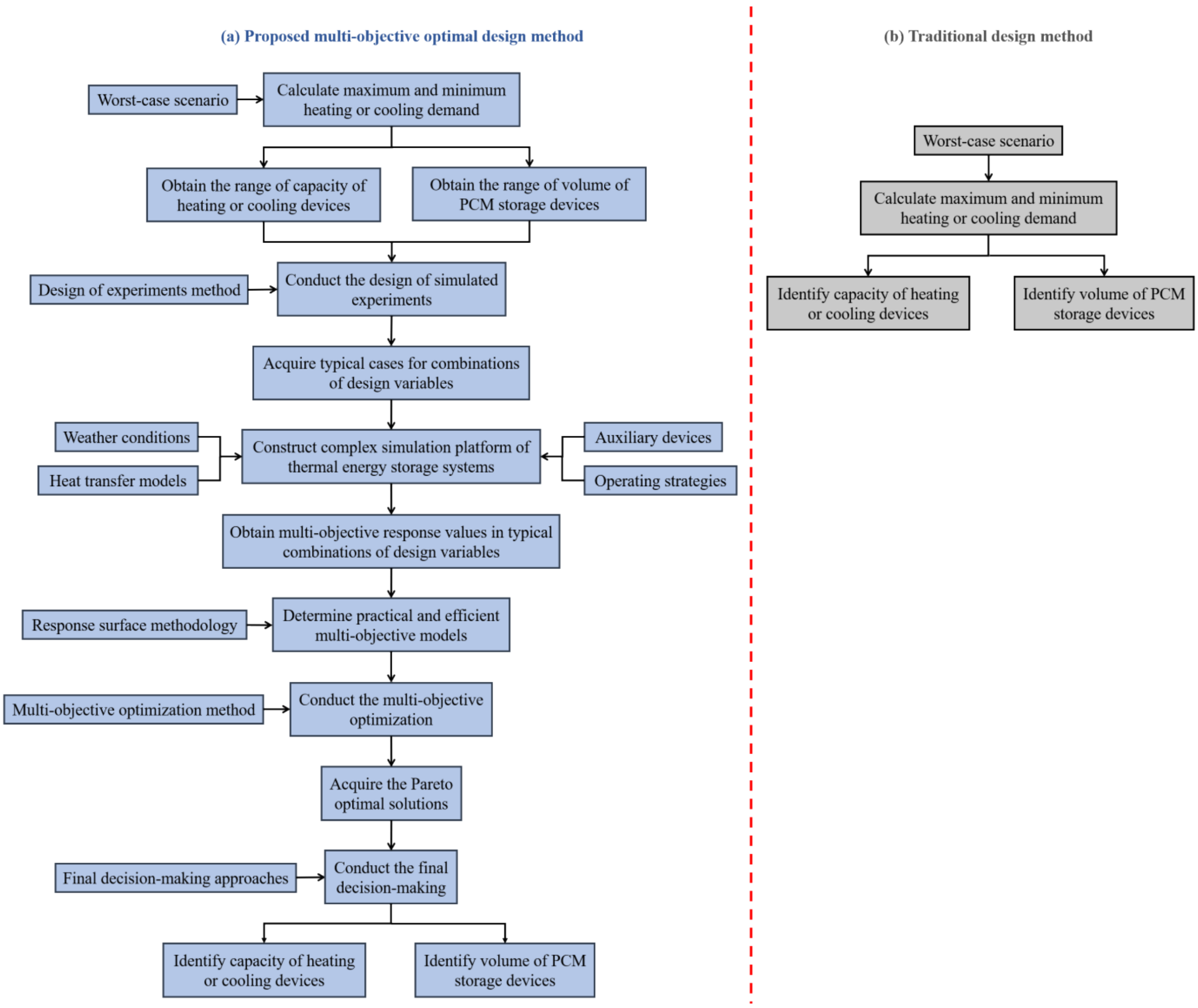

Fig. 1. Comparison between the (a) proposed multi-objective optimal design method and (b) traditional design method for thermal energy storage systems with PCM.

2.1. Design of simulated experiments (DOSE)

Design of experiment (DOE) contributes to conducting a detailed experimental plan that ensures the realization of high-quality and efficient experiments [48]. DOE has been extensively adopted for the design of real experiments, like characterization of polymer electrolyte membrane fuel cell [49] and lithium-ion batteries [50]. In addition, it has been used for the design of simulated experiments (DOSE), which can overcome the flaw of the real experiments that the results might be affected by the errors in the real conditions [26]. Central composite design (CCD) that is a popular design approach in the DOE is adopted in this study. The schematic for the two-factors CCD that is formulated according to design points containing factorial points, axial points, and central points is depicted in Fig. 2.

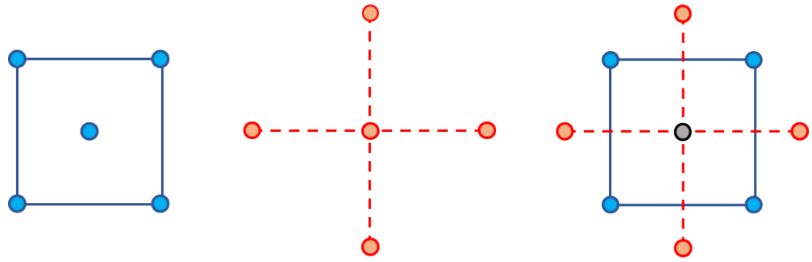

(a) **(b)** **(c)**

Fig. 2. Schematic diagram of two-factors CCD: (a) factorial points; (b) axial points; and (c) all points.

2.2. Response surface methodology

The RSM that utilizes the statistical and mathematical mechanism is adopted to establish the regression models of the response objectives. The general relationship between the response objectives and design variables is depicted as the following equation:

$$X = g(D_1, D_2, \ldots, D_s) + e_{rr} \tag{1}$$

where X represents the response objectives; $D_1, D_2, \ldots, D_s$ represents the design variables; and e_{rr} represents the random error. This equation usually consists of linear items, quadratic items, and interaction items, and hence it is also depicted as the following equation [25]:

$$X = c_{iv} + \sum_{r=1}^{u} c_r D_r + \sum_{r=1}^{u} c_{rr} D_r^2 + \sum_{r<n}^{u} c_{rn} D_r D_n + e_{rr} \tag{2}$$

where c_{iv} represents the intercept value; c_k represents the coefficient of the linear items; c_{rr} represents the coefficient of the quadratic items; and c_{rn} represents the coefficient of the interaction items.

2.3. Multi-objective optimization method

MOO is an efficient method to simultaneously optimize a variety of conflicting objectives in real-world engineering field [51]. The mathematical expression of a MOO problem is summarized as follows [52]:

$$\text{Find } \boldsymbol{z} = (z_l) \qquad \forall\, l = 1, 2, \ldots\ldots, L \tag{3}$$

$$\text{Maximize or Minimize } F_m(\boldsymbol{z}) \qquad \forall\, m = 1, 2, \ldots\ldots, M \tag{4}$$

Subject to:

$$G_p(\boldsymbol{z}) = 0 \qquad \forall\, p = 1, 2, \ldots\ldots, P \tag{5}$$

$$H_q(\boldsymbol{z}) \leq 0 \qquad \forall\, q = 1, 2, \ldots\ldots, Q \tag{6}$$

where $\boldsymbol{z}$ represents the vector of decision parameters; $F_m(\boldsymbol{z})$ represents the m_{th} objective function; $G_p(\boldsymbol{z})$ and $H_q(\boldsymbol{z})$ respectively represents the p_{th} equality and q_{th} inequality constraints; and L, M, P and Q respectively represents the number of decision parameters, objective functions, equality and inequality constraints.

Since no unique optimal solution that can minimize or maximize all the objective functions exists in the MOO problems, the Pareto optimal solutions (i.e. non-dominated solutions) are adopted to denote the best combinations of objective functions. For instance, a Pareto optimal curve for simultaneously minimizing two objective functions (i.e. f_1 and f_2) is depicted in Fig. 3. Red points in the Pareto curve denote Pareto optimal solutions; and blue points denote other solutions that are worse than optimal ones. The ideal and non-ideal solution points are adopted for identifying the lower and upper boundaries of Pareto optimal solutions. It should be noted that the ideal solution point is a “utopia point”, which is make up of individual minimum value in each objective [53, 54]. This is the reason why the ideal solution is in the ranges of unfeasible solutions.

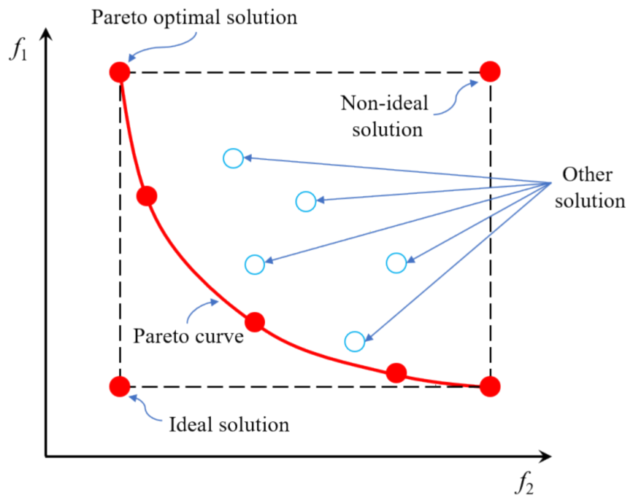

Fig. 3. Schematic diagram of Pareto optimal solutions for double-objective functions [53, 54].

NSGA-II that is regarded as a high-level generic algorithm is adopted to conduct the MOO. The fundamental flowchart of the NSGA-II, including the process of selection, crossover, and mutation is presented in Fig. 4.

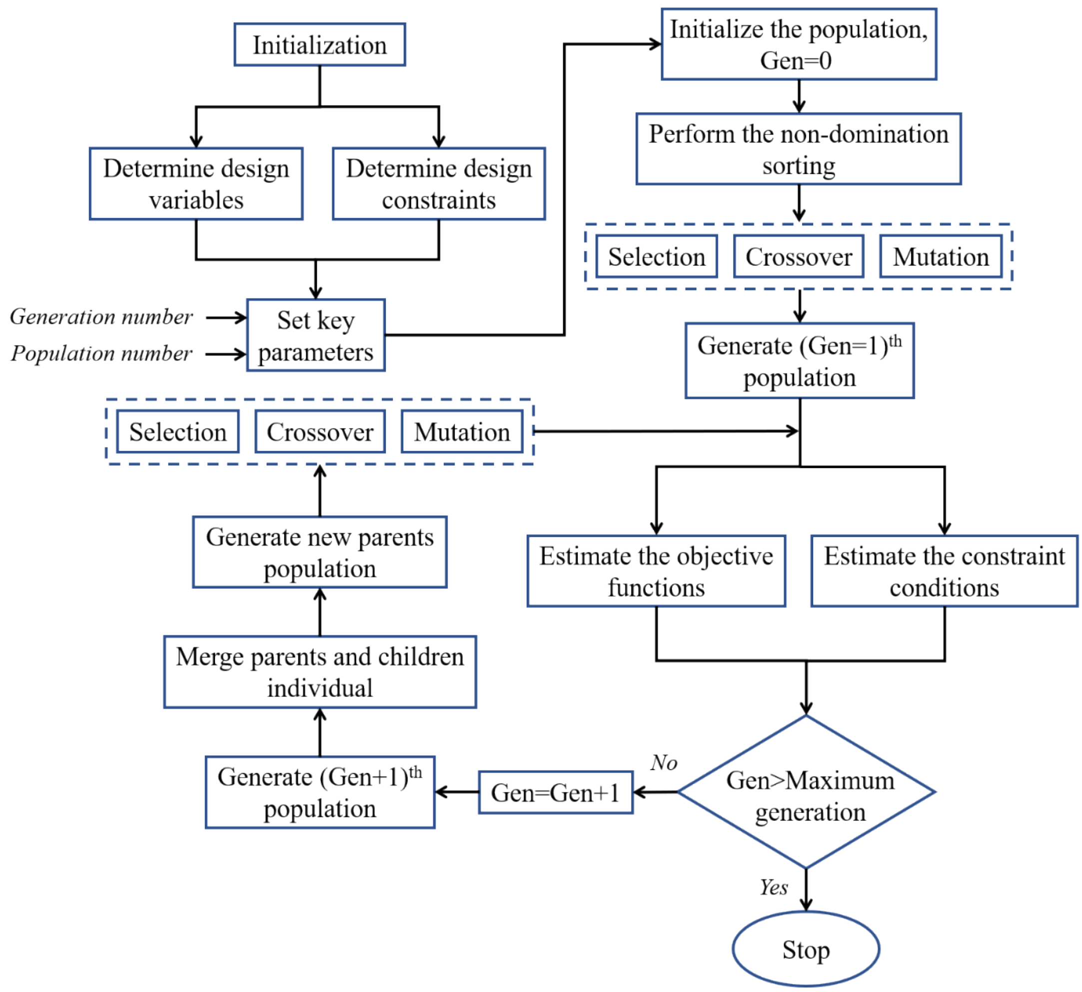

Fig. 4. Fundamental flowchart of the NSGA-II.

2.4. Final decision-making approaches

The significance of all the members in the Pareto optimal set are identical, and thus it is difficult to directly identify the single optimal solution for satisfying the practical requirement. To overcome this difficulty, a few typical FDM methods (e. g. LINMAP and TOPSIS approaches) are adopted to provide the final optimal solution for decision-makers in the MOO problem, depicted as follows:

- LINMAP decision-making approach [55, 56]

In the LINMAP approach, the Euclidian distance between each Pareto optimal and the ideal solution (DE_{r+}) is calculated by the following equation:

$$DE_{r+} = \sqrt{\sum_{s=1}^{M} \left(F_{rs} - F^{ideal}_{s}\right)^2} \qquad \forall\, r = 1, 2, \ldots\ldots, R \tag{7}$$

where R is the number of Pareto optimal solutions; F_{rs} and F^{ideal}_{s} are respectively the r_{th} and ideal value for the s_{th} objective. The solution that has a minimum DE_{r+} is considered as the final optimal solution, expressed as follows:

$$r_{final} = r \in \min\,(DE_{r+}) \quad (8)$$

● TOPSIS decision-making approach [57]

In the TOPSIS approach, the Euclidian distance between each Pareto optimal and the non-ideal solution (DE_{r-}) is calculated by the following equation:

$$DE_{r-} = \sqrt{\sum_{s=1}^{M}(F_{rs} - F^{non-ideal}_{s})^2} \qquad \forall\, r = 1, 2, \ldots\ldots, R \quad (9)$$

where $F^{non-ideal}_{s}$ is the non-ideal value for the s_{th} objective. The estimation indicator is the parameter (DE_r), which can be expressed as the following equation:

$$DE_r = \frac{DE_{r-}}{DE_{r+} + DE_{r-}} \quad (10)$$

The solution that has a maximum DE_r is selected as the final optimal solution, depicted as follows:

$$r_{final} = r \in \max\,(DE_r) \quad (11)$$

3. Case study

The OSP heating system that uses AHPs as the heating device, and PST as the thermal energy storage device, is selected as the case study in this study. The MOO of this system will be conducted to well illustrate the proposed multi-objective optimal design method of thermal energy storage systems.

3.1. Outdoor swimming pool heating system

The proposed heating system adopted in the OSP consists of thermal-insulation cover, PST, AHPs, pumps, heat exchangers and valves, etc. Fig. 5 depicts the schematic of the OSP heating system. The thermal-insulation cover is paved on the surface of the pool for reducing the heat loss when the OSP is closed. During the electric off-peak period, the AHPs and their corresponding pumps are switched on to store thermal energy into the PST. They are switched off when the temperature value of the PST reaches the design temperature 60^{o}C. In addition, the AHPs are responsible for preheating the water of the OSP during the electric off-peak period. The preheating process is regarded to be completed when the water temperature value of the OSP reaches the design temperature 28.5^{o}C. During the electric on-peak period, the heat stored by the PST is released into the OSP. The PI controller is adopted to continually adjust the water flow rate to maintain the water temperature of the OSP at the design temperature 28^{o}C.

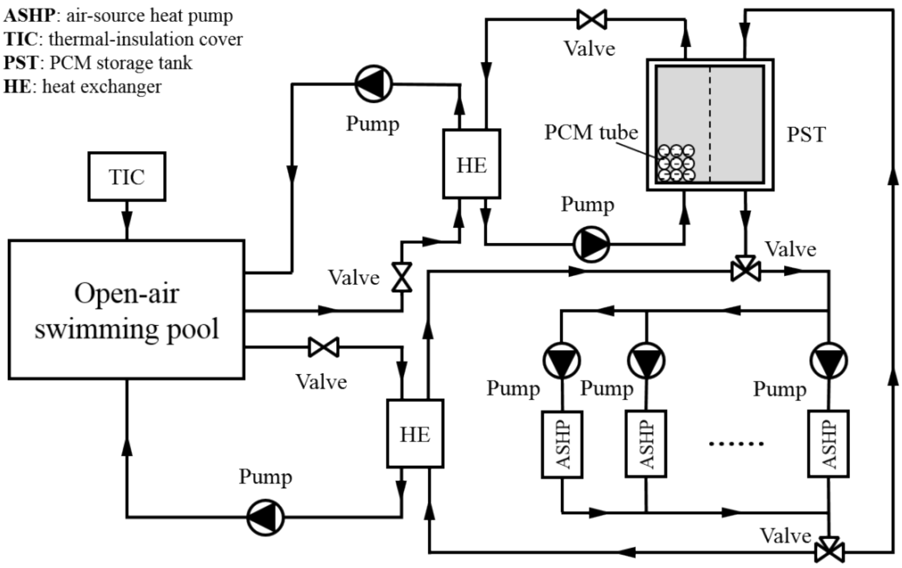

Fig. 5. Schematic of the proposed heating system adopted in the OSP.

The proposed heating system was applied in a typical OSP with a volume of 1963.5m^3 and a surface area of 1100m^2, which sites at the City University of Hong Kong (Cityu). This OSP suffers the difficulty that it cannot be used in winter season due to the cold weather condition, resulting in the waste of the space. Fig. 6 depicts the pictures of the closed OSP in the campus of Cityu. Hence, the proposed heating system was adopted to deal with this issue.

(a) (b)

Fig. 6. Pictures of the closed OSP in the campus of Cityu: (a) side view and (b) top view.

Fig. 7 depicts the water temperature profile of the OSP heating system within 24 hours. The open period of OSP is set from 12:00 to 20:00; and the preheating time of the OSP is set from 5:00 to 9:00. The starting time of the electric on-peak and off-peak period are 9:00 and 21:00, respectively. The design water temperature of 28.5°C and 26.6°C are predicted using the heat transfer model of the OSP based on the worst-case weather conditions.

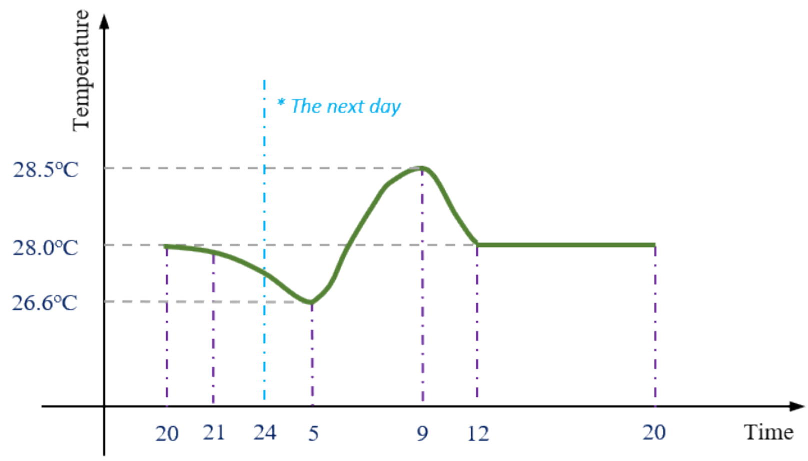

Fig. 7. Water temperature profile of the OSP heating system within 24 hours.

3.2. Design variables

The volume of PST (V_p) and heating capacity of AHPs (q_a) are considered as the design variables. Table 1 depicts the values of design variables in different design levels. The maximum values of V_p and q_a are selected as the high design level, which are identified according to the maximum thermal energy demands of the OSP during the open period and preheating period. The minimum values of V_p and q_a are selected as the low design level, which are identified according to 10% of the maximum thermal energy demands. The mean values between the maximum and minimum values of V_p and q_a are selected as the middle design level.

Table 1 Values of design variables in different design levels

Items	V_p(m^3)	q_a(kW)	Level
1	13.60	60.20	low
2	74.70	330.95	middle
3	135.80	601.70	high

Fig. 8 depicts the sizing method for identifying the maximum values of V_p and q_a. According to the weather data, temperature set point, and heat transfer model of OSP, the heat energy requirement during the open period and preheating period will be calculated. The maximum energy demand during the open period will be adopted to calculate the maximum value of V_p and maximum value of q_a for charging purpose. The maximum energy demand during the preheating period will be adopted to calculate the maximum value of q_a for preheating purpose. The maximum value between the maximum value of q_a for charging and preheating purpose will be considered as the final value of q_a.

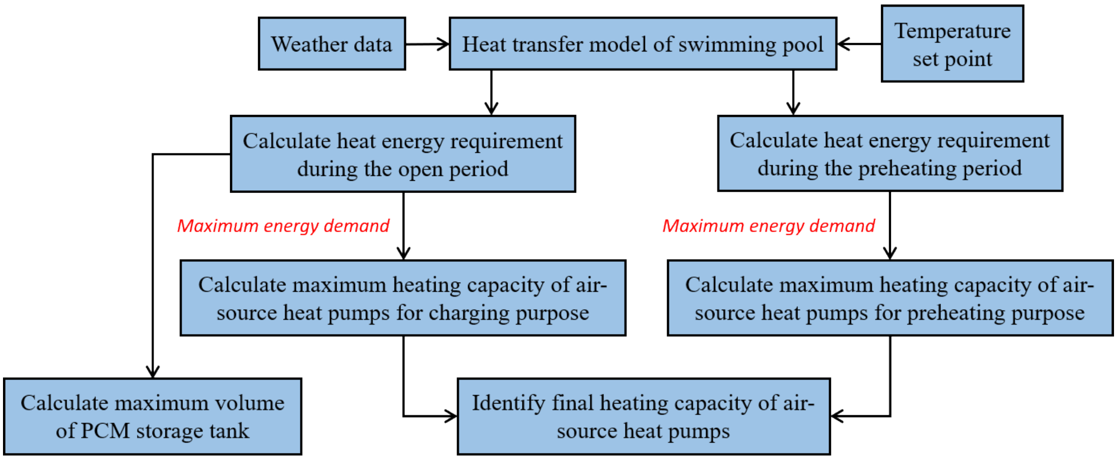

Fig. 8. Sizing method for identifying the maximum values of V_p and q_a.

Weather data of Hong Kong in ten cold seasons from 2003 to 2012 is adopted in the optimal design process. Fig. 9 depicts the average outdoor dry temperature, wet temperature, wind velocity, and solar irradiation in each cold season. The maximum and minimum dry temperature are 19.2°C and 17.8°C, occurring at 2006 and 2010, respectively. The maximum and minimum wet temperature are 16.9°C and 14.8°C, occurring at 2006 and 2010, respectively. The maximum and minimum wind velocity are 2.52m/s and 2.20m/s, occurring at 2008 and 2007, respectively. The maximum and minimum solar irradiation are 148W/m^2 and 106W/m^2, occurring at 2010 and 2009, respectively. Obviously, this belongs to the typical subtropical climate in cold season.

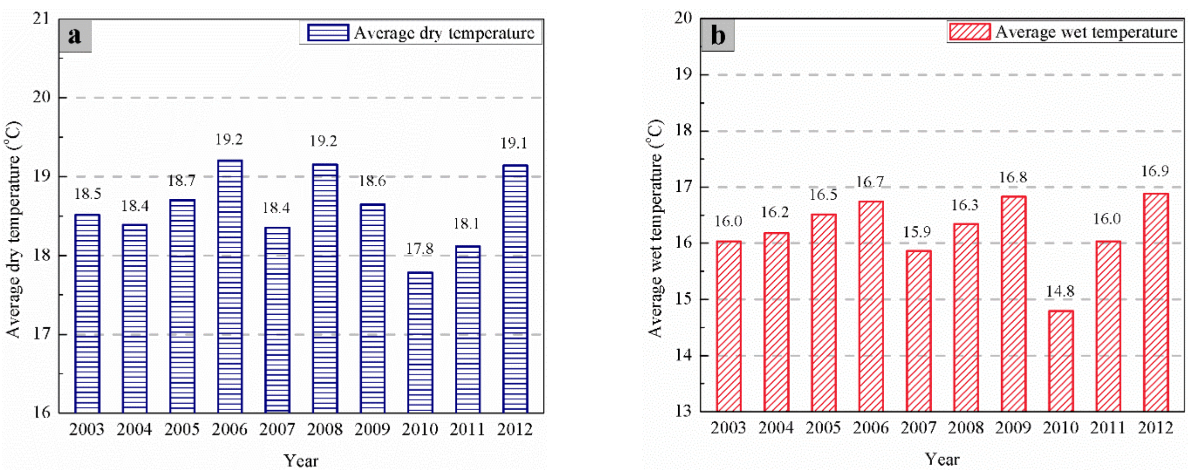

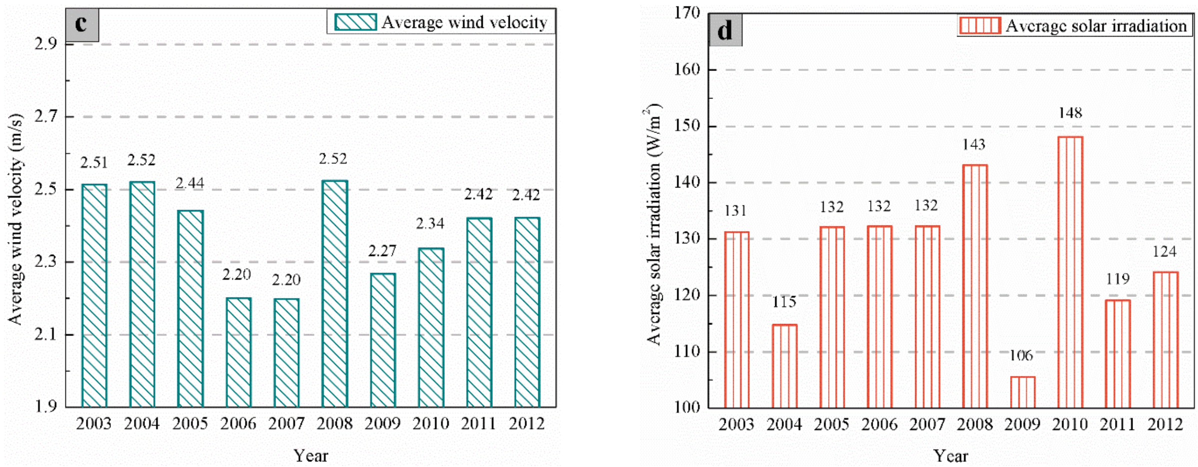

Fig. 9. Average outdoor (a) dry temperature; (b) wet temperature; (c) wind speed; and (d) solar irradiation in each cold season from 2003-2012.

3.3. Multiple optimization objectives

The objectives in the optimization include minimizing the thermal comfort unmet percentage (t_{cp}), minimizing the total energy use (e_t), and minimizing the lifecycle expense (c_l).

The thermal comfort unmet time percentage (t_{cp}) is considered as the reliability performance indicator of the system. It is the ratio between the total time that the thermal comfort requirement is unmet and the total time when the OSP is open in winter season (t_{ot}), which can be determined by the following formula:

$$t_{cp} = \frac{1}{t_{ot}} \int_0^{t_{ot}} c_{ut} dt \tag{12}$$

where c_{ut} represents an indicator applied to assess whether the thermal comfort requirement is satisfied, which can be determined as the following formula:

$$c_{ut} = \begin{cases} 0 & T_{pl} \geq T_{dpl} - \Delta_{ts} \\ 1 & T_{pl} < T_{dpl} - \Delta_{ts} \end{cases} \tag{13}$$

where T_{pl} and T_{dpl} respectively represent the temperature and the designed water temperature of the OSP; and Δ_{ts} represents a user-defined threshold.

The total energy use (e_t) is considered as the energy performance indicator. It is the sum of the energy use in each year within the entire lifetime of the project, which can be determined as the following formula:

$$e_t = \sum_{i=1}^{j} e_i \tag{14}$$

where e_i represents the energy use of the system in the i^{th} year within the lifetime of the year. It comprises the energy use of AHPs and pumps, calculated by the following formula:

$$e_i = e_{ai} + e_{pi} \tag{15}$$

where e_{ai} is the energy use of AHPs, which has the COP of 5.5; and e_{pi} is the energy us of pumps. The power of pumps (p_p) is related with water flow rate, shown as the following formula:

$$\frac{p_p}{p_d} = d_0 + d_1\frac{m_p}{m_d} + d_2\left(\frac{m_p}{m_d}\right)^2 + d_3\left(\frac{m_p}{m_d}\right)^3 \tag{16}$$

where m_p is the water flow rate; p_d is the designed power of pumps; m_d is the designed water flow rate; and d_0, d_1, d_2, and d_3 are the coefficients, which are 0, 0.0016, −0.0037, and 0.9671, respectively [58]. The p_d and m_d of pumps associated with AHPs are 5kW and 71.3kg/s, respectively; and the p_d and m_d of other pumps are 12kW and 213.9kg/s, respectively.

The lifecycle expense (c_l) is considered as the economic performance indicator. It is the sum of the initial expense and operational expense of the system within the entire lifetime of the project, which can be determined as the following formula:

$$c_l = c_{it} + c_{ot} \tag{17}$$

where c_{it} and c_{ot} respectively represent the initial expense and operating expense of the system. The c_{it} mainly consists of the initial investment of AHPs, thermal-insulation cover, PST, pumps, controllers, and heat exchangers, shown as the following formula:

$$c_{it} = c_{iap} + c_{itc} + c_{ipt} + c_{ip} + c_{icr} + c_{ihe} \tag{18}$$

where c_{iap}, c_{itc}, c_{ipt}, c_{ip}, c_{icr}, and c_{ihe} denote the initial cost of the AHPs, thermal-insulation cover, PST, pumps, controllers, and heat exchangers, respectively. Each item in the Eqn. (18) is calculated according to the corresponding unit cost, depicted in Table 2. It should be noted that in this study V_p and q_a are considered as design variables, which means that during the optimal design process they are unfixed. Thus, c_{iap} and c_{ipt} are unfixed during the optimal design process. The quantity of thermal-insulation cover, pumps, controllers, and heat exchangers are considered as constant in different design cases during the optimization process. Thus, c_{itc}, c_{ip}, c_{icr}, and c_{ihe} are constant during the optimization process.

Table 2 Unit costs used in the initial cost

Items	Unit	Cost ($/Unit)
c_{iap}	kW	165
c_{itc}	m^2	4
c_{ipt}	m^3	316
c_{ip}	-	663
c_{icr}	-	3,331
c_{ihe}	-	780

The c_{ot} occurring within the lifetime of the project can be determined as the following formula [44]:

$$c_{ot} = c_{o1}\sum_{i=1}^{j}\left(\left(1 + r_c\right)/\left(1 + a_c\right)\right)^{i-1} \tag{19}$$

where c_{o1} represents the operating expense in the first year of the lifecyle; and r_c and a_c represent the rate for the increase of the electricity and the discount in the market, respectively.

The operating cost (c_o) consists of the cost in the on-peak period and off-peak period, calculated by the following equation:

$$c_o = c_{dc,od} + c_{dc,fd} + c_{ec,od} + c_{ec,fd} \tag{20}$$

where od and fd denote the on-peak and off-peak period, respectively; and dc and ec denotes the cost caused by the demand and energy charge, respectively.

Table 3 Electricity price referred to the bulk tariff in the CLP [59]

	On-peak period		Off-peak period	
Demand	Range (kW)	Charge ($/kW)	Range (kW)	Charge ($/kW)
charge	[0, 650)	8.89	[0, d_{onk})	0
	[650, ∞)	8.50	[d_{onk}, ∞)	3.48
Energy charge	Range (MWh)	Charge ($/MWh)	Range (MWh)	Charge ($/MWh)
	[0, 200)	9.59×10^{-5}	-	8.59×10^{-5}
	[200, ∞)	9.39×10^{-5}	-	-

d_{onk}: on-peak billing demand

3.4. Simulation platform

Two popular simulation software including MATLAB and TRNSYS were adopted to construct the simulation platform of the OSP heating system. The operation of the system was performed in the environment provided by the TRNSYS 17. The AHPs, heat exchangers, pumps, mixing valves, diverting valves, and PID controller were simulated by Type 941, Type 91, Type 3b, Type 649, Type 647, and Type 23 in the TRNSYS, respectively. Heat transfer models of the OSP and PST were coded using the MATLAB programs. Type 155 was responsible for linking them into the TRNSYS. The heat transfer model of the OSP was adopted to calculate the water temperature of the OSP, which was determined by the following equation [60, 61]:

$$\rho_{wt} \cdot c_{wt} \cdot V_{pl} \cdot \frac{dT_{pl}}{dt} = q_{pl} \tag{21}$$

where V_{pl} represents the volume of the OSP; and q_{pl} represents the total heat flux of the OSP. During the open period of the OSP, q_{pl} consists of heat gained from the solar [44] and storage tank, and heat loss from the evaporation [62], radiation [63], convection [44], conduction [64], and refilling fresh water [60]. During the closing period of the OSP, q_{pl} consists of heat gained from the AHPs, and heat loss from the conduction [64] and the cover.

The heat transmission model of the PST was proposed on the basis of the following assumptions: (1) no thermal energy was generated inside the PCM tubes; (2) no thermal energy was lost from the PST to surrounding environment; (3) thermo-physical parameters of the PCM and water were not influenced by their temperature [65]; (4) only the temperature variations along the direction of the water flow were taken into account; (5) during the process of phase change transition the temperature of PCM was fixed. It should be noted that the third assumption suggests that during the simulation the specific heat and thermal conductivity are fixed values in the solid phase, and they are also fixed values in the liquid phase. The governing equations for describing the diabatic process between the PCM and water were depicted from the water and PCM side. For the water side, it is determined by the following equation:

$$\rho_{wt} \cdot c_{wt} \cdot \varepsilon_{wt} \cdot (\frac{\partial T_{wt}}{\partial t} + \cdot u_{wt} \cdot \frac{\partial T_{wt}}{\partial x}) = k_{wt} \cdot \varepsilon_{wt} \cdot \frac{\partial^2 T_{wt}}{\partial^2 x} + h_{wp} \cdot (T_{pcm} - T_{wt}) \quad (22)$$

where u_{wt} represents the mean velocity of water; and k_{wt} represents the thermal conductivity of water; ε_{wt} represents the water fraction; T_{pcm} represents the temperature of PCM; t and x represents the time and distance, respectively. For the PCM side, it is depicted as the following equation:

$$\rho_{pcm} \cdot (1 - \varepsilon_{wt}) \cdot \frac{\partial H_{pcm}}{\partial t} = h_{wp} \cdot (T_{pcm} - T_{wt}) \quad (23)$$

where H_{pcm} represents the enthalpy of PCM. These two equations are discretized adopting the finite difference approach [65], and the discrete polynomial equations are solved and coded adopting MATLAB programs. The sodium acetate trihydrate that was a type of inorganic PCM was used in this study, since it has a large latent heat. Its thermo-physical parameters used during the simulation process referred to the values presented in the study of Cunha and Eames [66], shown in Table 4.

Table 4 Thermo-physical parameters of sodium acetate trihydrate [66]

Properties	Values
Melting temperature	58°C
Latent heat	266kJ/kg
Density	1450kg/m^3
Solid specific heat	1.68kJ/(kg·K)
Liquid specific heat	2.37kJ/(kg·K)
Solid thermal conductivity	0.43 W/(m·K)
Liquid thermal conductivity	0.34W/(m·K)

4. Results and discussion

4.1. Validation of main heat transfer models

In our previous study [47], the numerical results of the heat transfer model of the PST and OSP have been compared with the experimental results in the study of Watanabe et al. [67] and Ruiz et al. [63], respectively. The parameters and work conditions in the simulation and experiments were same. The average relative error (ε_{ae}) between the numerical and experimental results was used to estimate the accuracy of the models, which is calculated by the following equation:

$$\varepsilon_{ae} = \frac{1}{n}\sum_{j=1}^{j=n}\left|\frac{T_{ex,j} - T_{si,j}}{T_{ex,j}}\right| \times 100\% \tag{24}$$

where n denotes the number of experimental samples; and $T_{si,j}$ and $T_{ex,j}$ denote the simulated and experimental temperature values, respectively. The ε_{ae} for the heat transfer model of the PST and OSP was 3.97% and 0.65%, respectively, which indicated that the heat transfer model of the PST and OSP were reliable and correct.

4.2. Analysis of variance

The CCD-based DOSE plan of the system was conducted by the software of Design-Expert. Table 5 depicts the CCD-based DOSE with 13 design cases and the corresponding simulation results generated from the constructed simulation platform.

Table 5 CCD-based DOSE and corresponding simulation results

Case	V_p (m^3)	q_a (kW)	t_{cp} (×0.01%)	e_t (MWh)	c_l ($)
1	135.8	601.7	0	4,353.7	782,254
2	13.6	60.20	773.46	901.8	155,667
3	74.7	330.95	1.84	2,934.5	490,461
4	74.7	60.20	769.01	882.5	171,817
5	74.7	330.95	1.84	2,934.5	490,461
6	135.8	330.95	0	2,962.2	511,833
7	74.7	601.70	0.34	4,300.3	758,932
8	13.6	601.70	104.09	3,474.1	679,628
9	74.7	330.95	1.84	2,934.5	490,461
10	135.8	60.20	766.66	874.4	189,782
11	74.7	330.95	1.84	2,934.5	490,461
12	74.7	330.95	1.84	2,934.5	490,461
13	13.6	330.95	228.14	2,337.8	429,018

According to the CCD-based DOSE plan, typical regression models including linear, 2FI and quadratic model was generated. The predicted R^2 of linear, 2FI and quadratic model for the t_{cp} were 0.5656, 0.5198, and 0.9791, respectively. The predicted R^2 of linear, 2FI and quadratic model for the e_t were 0.9318, 0.9411, and 0.9926, respectively. The predicted R^2 of linear, 2FI and quadratic model for the c_l were 0.9881, 0.9899, and 0.9987, respectively. Hence, the fitting degree of the quadratic models for the response objectives were better than that of linear model and 2FI model.

The AOVA of the quadratic models for the response objectives were conducted to assess the significance of each item in the models and realize the establishment of the regression models, mainly judged by the values of P and F. The higher values of F and lower values of P indicated that the corresponding model items were more significant. In addition, the model items with the value of P that is less than 0.05 were statistically important. Table 6 depicts the ANOVA for the t_{cp}. The linear item of q_a have the maximum F value with 357.10 and the minimum P value with less than 0.0001, and hence it is considered as the most significant item in the regression model. The sequence for the significance of the items (from large to small) was q_a, q_a^2, V_p, V_p^2, and $V_p q_a$. Table 7 depicts the ANOVA for the e_t. The linear item of q_a have the maximum F value with 1485.53 and the minimum P value with less than 0.0001, and hence it is considered as the most significant item in the regression model. The sequence for the significance of the items (from large to small) was q_a, V_p, q_a^2, $V_p q_a$, and V_p^2. Table 8 depicts the ANOVA for the c_l. The linear item of q_a have the maximum F value with 8981.46 and the minimum P value with less than 0.0001, and hence it is considered as the most significant item in the regression model. The sequence for the significance of the items (from large to small) was q_a, V_p, q_a^2, $V_p q_a$, and V_p^2.

Table 6 AOVA for the t_{cp}

Source	Sum of squares	DF	Mean square	F	P
Model	0.013	5	2.568×10^{-3}	113.18	< 0.0001
V_p	1.916×10^{-4}	1	1.916×10^{-4}	8.44	0.0228
q_a	8.101×10^{-3}	1	8.101×10^{-3}	357.10	< 0.0001
$V_p q_a$	2.367×10^{-5}	1	2.367×10^{-5}	1.04	0.3411
V_p^2	1.384×10^{-4}	1	1.384×10^{-4}	6.10	0.0429
q_a^2	3.219×10^{-3}	1	3.219×10^{-3}	141.89	< 0.0001
Residual	1.588×10^{-4}	7	2.269×10^{-5}	-	-
Lack of Fit	$1.588\text{E}\times10^{-4}$	3	5.293×10^{-5}	-	-
Pure Error	0	4	0	-	-
Cor Total	0.013	12	-	-	-

Table 7 AOVA for the e_t

Source	Sum of squares	DF	Mean square	F	P
Model	2.094×10^{6}	5	4.189×10^{5}	321.26	< 0.0001
V_p	47093.82	1	47093.82	36.12	0.0005
q_a	1.937×10^{6}	1	1.937×10^{6}	1485.53	< 0.0001
$V_p q_a$	26661.73	1	26661.73	20.45	0.0027
V_p^2	20455.52	1	20455.52	15.69	0.0055
q_a^2	31712.68	1	31712.68	24.32	0.0017
Residual	9126.68	7	1303.81	-	-
Lack of Fit	9126.68	3	3042.23	-	-
Pure Error	0	4	0	-	-
Cor Total	2.103×10^{6}	12	-	-	-

Table 8 AOVA for the c_l

Source	Sum of squares	DF	Mean square	F	P
Model	2.937×10^{13}	5	5.873×10^{12}	1843.09	< 0.0001
V_p	4.754×10^{11}	1	4.754×10^{11}	149.18	< 0.0001
q_a	2.862×10^{13}	1	2.862×10^{13}	8981.46	< 0.0001
$V_p q_a$	6.944×10^{10}	1	6.944×10^{10}	21.79	0.0023
V_p^2	4.668×10^{10}	1	4.668×10^{10}	14.65	0.0065
q_a^2	7.875×10^{10}	1	7.875×10^{10}	24.71	0.0016
Residual	2.231×10^{10}	7	3.187×10^{9}	-	-
Lack of Fit	2.231×10^{10}	3	7.435×10^{9}	-	-
Pure Error	0	4	0	-	-
Cor Total	2.939×10^{13}	12	-	-	-

4.3. Regression model of multiple optimization objectives

The quadratic regression models of the response objectives that were constructed using the response surface methodology can be summarized as the following equation:

$$X = c_0 + c_1 \cdot V_p + c_2 \cdot q_a + c_{1,2} \cdot V_p q_a + c_{1,1} \cdot V_p^2 + c_{2,2} \cdot q_a^2 \tag{25}$$

Table 9 depicts the corresponding item coefficients in the quadratic models for the response objectives including thermal comfort unmet time percentage (t_{cp}), total energy use (e_t), and lifecycle expense of the system (c_l). Fig. 10 depicts the variations of normal probability with internally studentized residuals in different response objectives including (a) t_{cp}; (b) e_t; and (c) c_l. It could be found that the points were well distributed surrounding the red straight line, indicating that the errors in all the response models satisfied the normal distribution. In addition, it could be seen that there was a good agreement between the simulation results and predicted results. This suggested that all the quadratic regression models were reliable and accurate.

Table 9 Item coefficients in the regression models of response objectives

	t_{cp}	e_t	c_l
c_0	0.111	82.202	5.024×10^{5}
c_1	-3.271×10^{-4}	3.261	7173.748
c_2	-4.330×10^{-4}	2.697	8996.352
$c_{1,2}$	-1.470×10^{-7}	4.935×10^{-3}	7.964
$c_{1,1}$	1.896×10^{-6}	-0.023	-34.824
$c_{2,2}$	4.657×10^{-7}	-1.462×10^{-3}	-2.303

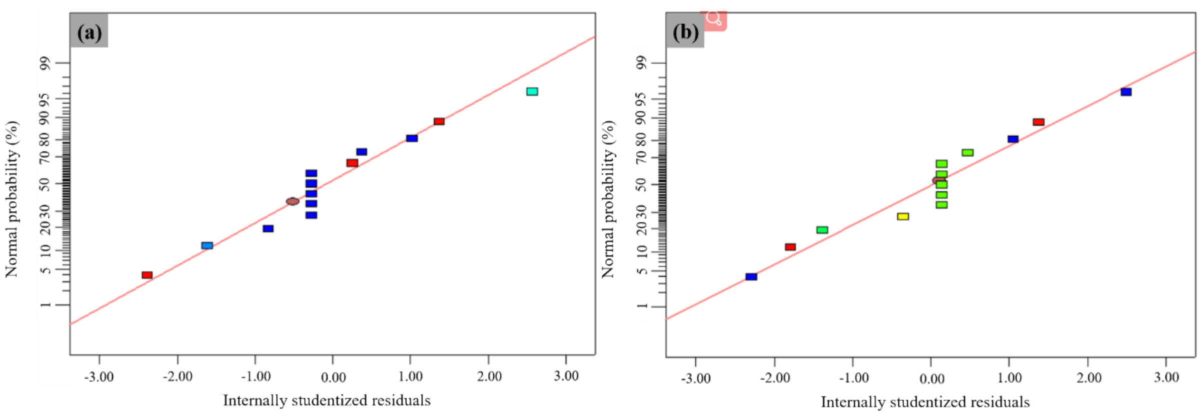

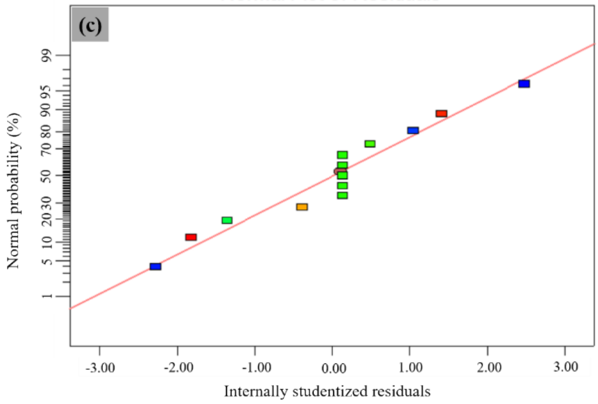

Fig. 10. Variations of normal probability with internally studentized residuals in different response objectives: (a) t_{cp}; (b) e_t; and (c) c_l.

4.4. Multi-objective optimization and final decision-making

4.4.1 Double-objective optimization

Three sets of double-objective optimization were conducted: the optimization objectives of the first set were minimizing the thermal comfort unmet time percentage (t_{cp}) and minimizing the total energy use (e_t); the optimization objectives of the second set were minimizing the t_{cp} and minimizing the lifecycle expense of the system (c_l); and the optimization objectives of the third set were minimizing the c_l and minimizing the e_t. The design constraint was that the t_{cp} should be less than 2%, when the third set of double-objective optimization was conducted. Fig. 11 depicts the Pareto optimal solutions for the double-objective optimization. As depicted in Fig. 11 (a), the value of the e_t was 2,983.3MWh when the value of the t_{cp} was 0%; and the value of the e_t was 787.2MWh when the value of the t_{cp} was 8.25%. As depicted in Fig. 11 (b), the value of the c_l was \$499,967 when the value of the t_{cp} was 0%; and the value of the c_l was \$147,329 when the value of the t_{cp} was 8.25%. As depicted in Fig. 11 (c), the value of the e_t was 2278.4MWh when the value of the c_l was \$379,039; and the value of the e_t was 2227.0MWh when the value of the c_l was \$395,638. To further perform the FDM using the LINMAP and TOPSIS approaches, ideal and non-ideal solution should be identified. The ideal and non-ideal solution in the first set were respectively the solution that the value of the t_{cp} was 0% and the value of the e_t was 787.2MWh, and the solution that the value of the t_{cp} was 8.25% and the value of the e_t was 2,983.3MWh. The ideal and non-ideal solution in the second set were respectively the solution that the value of the t_{cp} was 0% and the value of the c_l was \$147,329, and the solution that the value of the t_{cp} was 8.25% and the value of the c_l was \$499,967. The ideal and non-ideal solution in the third set were respectively the solution that the value of the c_l was \$379,039 and the value of the e_t was 2227.0MWh, and the solution that the value of the c_l was \$395,638 and the value of the e_t was 2278.4MWh. Fig. 11 also depicts the final optimal solutions identified using FDM methods. The results of the final optimal solutions for the double-objective optimization are depicted in Table 10. Table 10 also presents the comparison between the output values generated by surrogated models and simulation platform in different final optimal solutions. The t_{cp}, e_t, and c_l were the thermal comfort unmet time percentage, total energy use, and lifecycle expense generated by surrogate models; and the t_{rcp}, e_{rt}, and c_{rl} were the thermal comfort unmet time percentage, total energy use, and lifecycle expense generated by simulation platform.

Table 10 Results of final optimal solutions for the double-objective optimization

	V_p (m^3)	q_a (kW)	t_{cp} (%)	e_t (MWh)	c_l (\$)	t_{rcp} (%)	e_{rt} (MWh)	c_{rl} (\$)
LINMAP solution for e_t and t_{cp}	13.7	273.0	2.30	2,134.5	378,079	3.09	2,148.3	379,450
TOPSIS solution for e_t and t_{cp}	24.0	315.4	1.30	2,471.5	431,999	1.35	2,568.4	440,280
LINMAP solution for c_l and t_{cp}	59.4	236.2	2.00	2,276.4	378,820	1.06	2,505.6	395,386
TOPSIS solution for c_l and t_{cp}	67.5	279.1	1.04	2,581.5	430,226	0.23	2,718.2	440,185
LINMAP solution for e_t and c_l	38.3	254.2	2.00	2,256.8	382,398	0.88	2,627.9	412,125
TOPSIS solution for e_t and c_l	42.1	250.2	2.00	2,261.3	381,350	0.90	2,608.6	408,509

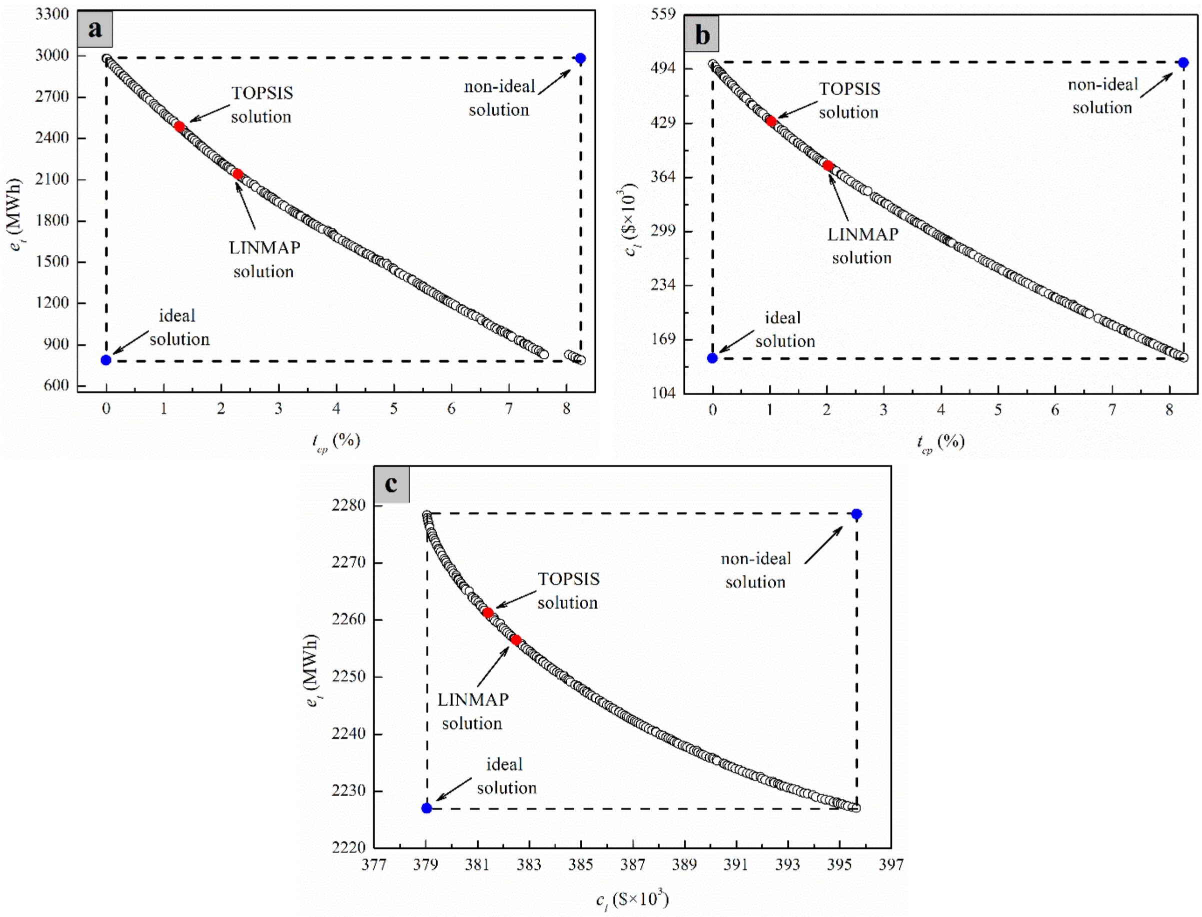

Fig. 11. Pareto and final optimal solutions identified by FDM methods for double-objective optimization: (a) variations of e_t with t_{cp}; (b) variations of c_l with t_{cp}; and (c) variations of e_t with c_l.

4.4.2 Triple-objective optimization

The triple-objective optimization where the objectives are minimizing the thermal comfort unmet time percentage (t_{cp}), minimizing the total energy use (e_t) and minimizing the lifecycle expense of the system (c_l). Fig. 12 depicts the Pareto optimal solutions and final optimal solutions identified by FDM methods for triple-objective optimization. It is observed that the values of the e_t and c_l were respectively 2,980.6MWh and \$499,954 when the value of the t_{cp} was 0%; and the values of the e_t and c_l were respectively 787.2MWh and \$147,329 when the value of the t_{cp} was 8.25%. Thus, the ideal and non-ideal solutions in triple-objective optimization were respectively the solution that the values of the t_{cp}, e_t and

c_l were 0%, 787.2MWh and \$147,329, and the solution that the values of the t_{cp}, e_t and c_l were 8.25%, 2,980.6MWh and \$499,954. The results of the final optimal solutions in the triple-objective optimization were depicted in Table 11. Table 11 also presents the comparison between the output values generated by surrogated models and simulation platform in different final optimal solutions.

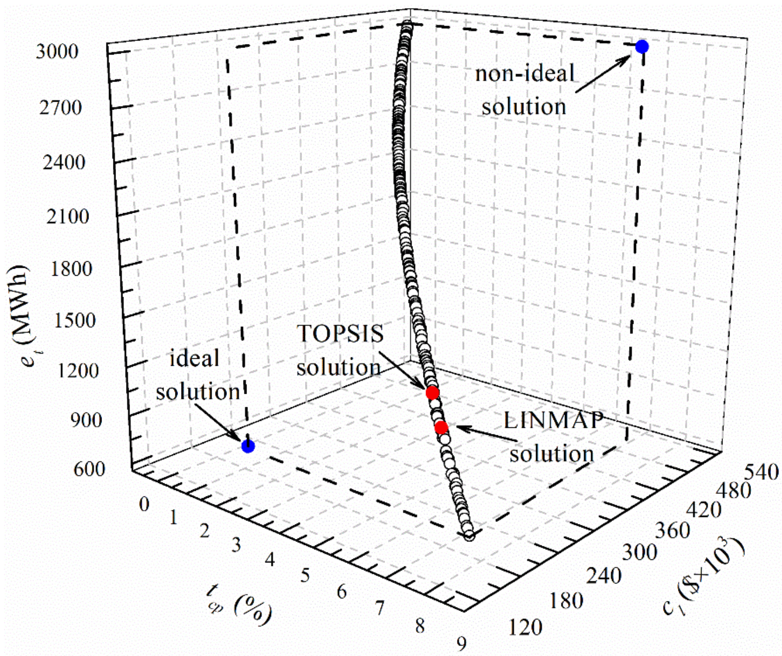

Fig. 12. Pareto and final optimal solutions identified by FDM methods for triple-objective optimization.

Table 11 Results of final optimal solutions in the triple-objective optimization

	V_p (m^3)	q_a (kW)	t_{cp} (%)	e_t (MWh)	c_l (\$)	t_{rcp} (%)	e_{rt} (MWh)	c_{rl} (\$)
LINMAP solution	62.4	242.2	1.84	2,328.1	387,189	0.87	2,535.4	402,252
TOPSIS solution	45.1	203.4	3.01	1,988.4	333,137	2.36	2,321.2	358,886

4.5. Optimal results analysis

The design variables of the final optimal solutions that were depicted in Table 12, were input into the simulation platform to analyze the energy and economic performance.

Table 12 Eight cases with the final optimal solutions

Case	solutions	V_p (m^3)	q_a (kW)
1	LINMAP solution for e_t and t_{cp}	13.7	273.0
2	TOPSIS solution for e_t and t_{cp}	24.0	315.4
3	LINMAP solution for c_l and t_{cp}	59.4	236.2
4	TOPSIS solution for c_l and t_{cp}	67.5	279.1
5	LINMAP solution for e_t and c_l	38.3	254.2
6	TOPSIS solution for e_t and c_l	42.1	250.2
7	LINMAP solution for e_t, c_l and t_{cp}	62.4	242.2
8	TOPSIS solution for e_t, c_l and t_{cp}	45.1	203.4

To evaluate the energy performance, the energy saving ratio (e_r) that was defined as the ratio between saving energy use of the system in comparison with the traditional system and that of the traditional system, was selected as the indicator. Fig. 13 presents the ten-years average e_r in eight cases with final optimal solutions. The maximum e_r was 80.2%, occurring in Case 1; and the minimum e_r was 75.0%, occurring in Case 4. The e_r in Case 2, Case 3, Case 5, Case 6, Case 7, and Case 8 was 76.4%, 77.0%, 75.9%, 76.0%, 76.7%, and 78.7%, respectively. If the final selection principle to was to obtain the maximum ten-years average e_r, the Case 1 will be identified as the most suitable final optimal solution.

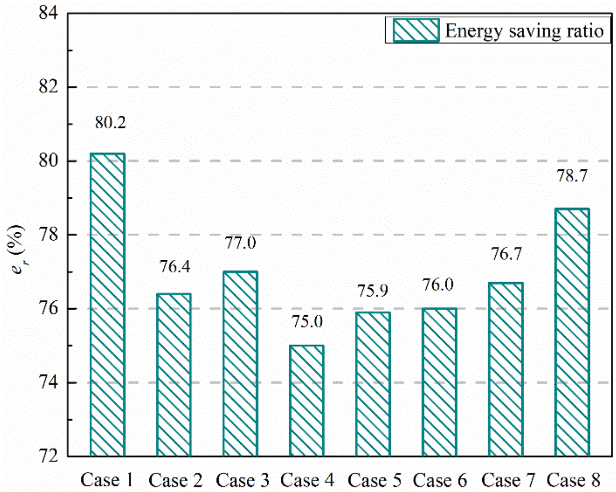

Fig. 13. Ten-years average e_r in eight cases with final optimal solutions.

To evaluate the economic performance, the operating cost saving ratio (o_r) that was defined as the ratio between saving operating cost of the system in comparison with the traditional system and that of the traditional system, was selected as the indicator. Fig. 14 presents the ten-years average o_r in eight cases with final optimal solutions. The maximum o_r was 85.4%, occurring in Case 1; and the minimum o_r was 82.8%, occurring in Case 4. The o_r in Case 2, Case 3, Case 5, Case 6, Case 7, and Case 8 was 83.0%, 84.1%, 83.2%, 83.4%, 83.9%, and 85.2%, respectively. If the final selection principle to was to obtain the maximum ten-years average o_r, the Case 1 will be identified as the most suitable final optimal solution.

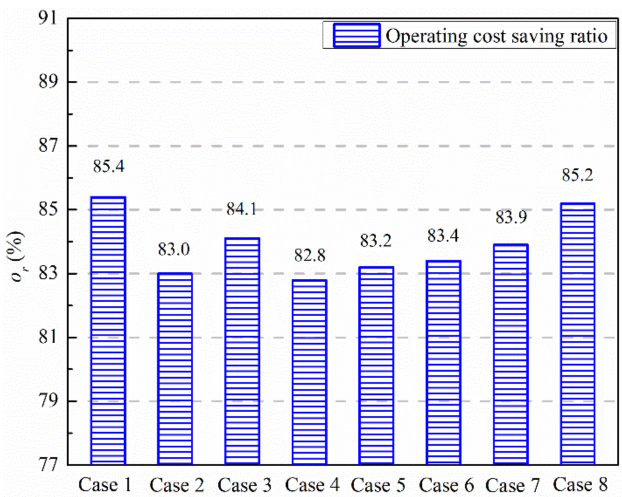

Fig. 14. Ten-years average o_r in eight cases with final optimal solutions.

The simple payback period of the system (s_p) in eight cases with final optimal solutions were calculated, shown in Fig. 15. The longest s_p was 1.24 years, occurring in Case 2; and the shortest s_p was 0.88 years, occurring in Case 8. The s_p in Case 1, Case 3, Case 4, Case 5, Case 6, and Case 7 was 1.05, 1.04, 1.22, 1.06, 1.06, and 1.07 years, respectively. If the final selection principle to was to obtain the shortest s_p, the Case 8 will be identified as the most suitable final optimal solution.

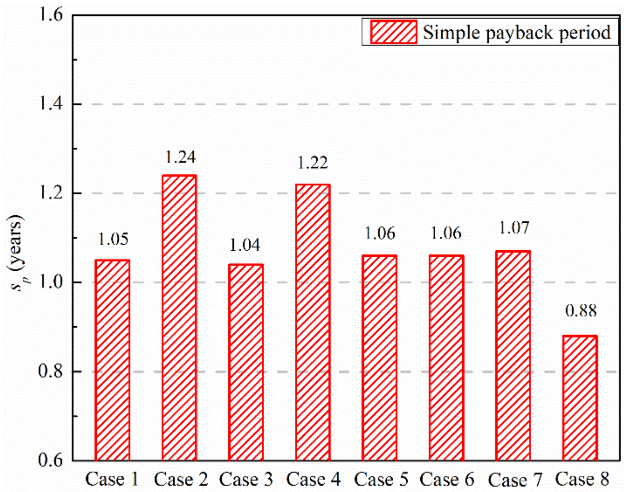

Fig. 15. s_p in eight cases with final optimal solutions.

5. Conclusions

An approach of conducting the MOO for the TES systems with PCM was proposed in this study. To better illustrate the proposed approach, a case study of optimizing the design of an OSP heating system with PST was presented. The CCD approach in the DOE was adopted to design the cases that were made up of design variables and optimization objectives. The volume of the PST and the heating capacity of the AHPs were selected as the design variables. Minimizing the thermal comfort unmet time percentage, minimizing the energy use, and minimizing the lifecycle expense of the system were selected as the optimization objectives. The RSM was used to develop the surrogated models of the optimization objectives according to the design cases. The AOVA indicated that the fitting degree between the predicted results and simulated results of the quadratic models for the response objectives were better than that of linear model and 2FI model, which suggested that the quadratic models were reliable and accurate. The double-objective optimization and triple-objective optimization of the system were conducted based on the quadratic models and NSGA-II, and the Pareto optimal solutions were obtained. The final optimal solutions were identified using LINMAP and TOPSIS methods, respectively. The performance analysis of the OSP heating system with different final optimal solutions was conducted. The results indicated that the ten-years average e_r of the system in eight different final optimal solutions was 80.2%, 76.4%, 77.0%, 75.0%, 75.9%, 76.0%, 76.7%, and 78.7%, respectively; the ten-years average o_r of the system in eight different final optimal solutions was 85.4%, 83.0%, 84.1%, 82.8%, 83.2%, 83.4%, 83.9%, and 85.2%, respectively; and the s_p of the system in eight different final optimal solutions was 1.05, 1.24, 1.04, 1.22, 1.06, 1.06, 1.07, and 0.88 years, respectively. Hence, it was suggested that this proposed method could effectively perform the multi-objective optimal design for the OSP heating system, and it also provided a useful guideline for the optimal design of the TES systems with PCM.

Acknowledgments

The authors sincerely thank the anonymous reviewers for their time and effort. In addition, the authors appreciate the support of Dr. Gongsheng Huang.

References

[1] Reddy KS, Mudgal V, Mallick TK. Review of latent heat thermal energy storage for improved material stability and effective load management. Journal of Energy Storage. 2018;15:205-27.

[2] Du Y, Blocken B, Pirker S. A novel approach to simulate pollutant dispersion in the built environment: Transport-based recurrence CFD. Building and Environment. 2020;170.

[3] B.V Rm, Gumtapure V. Thermal property study of fatty acid mixture as bio-phase change material for solar thermal energy storage usage in domestic hot water application. Journal of Energy Storage. 2019;25.

[4] Mehta DS, Solanki K, Rathod MK, Banerjee J. Thermal performance of shell and tube latent heat storage unit: Comparative assessment of horizontal and vertical orientation. Journal of Energy Storage. 2019;23:344-62.
[5] Yantong L, Quan Z, Xiaoqin S, Yaxing D, Shuguang L. Optimization on Performance of the Latent Heat Storage Unit (LHSU) in Telecommunications Base Stations (TBSs) in China. Energy Procedia. 2015;75:2119-24.
[6] Dardir M, Panchabikesan K, Haghighat F, El Mankibi M, Yuan Y. Opportunities and challenges of PCM-to-air heat exchangers (PAHXs) for building free cooling applications—A comprehensive review. Journal of Energy Storage. 2019;22:157-75.
[7] Ding Z, Jiang Z, Liu W, Wang J, Zhang Y. The influence of channels per square inch on the freezing progress of the square copper column array water composite PCM. Journal of Energy Storage. 2019;26.
[8] Kadivar MR, Moghimi MA, Sapin P, Markides CN. Annulus eccentricity optimisation of a phase-change material (PCM) horizontal double-pipe thermal energy store. Journal of Energy Storage. 2019;26.
[9] Xu T, Li Y, Chen J, Liu J. Preparation and thermal energy storage properties of LiNO 3 -KCl-NaNO 3 /expanded graphite composite phase change material. Solar Energy Materials and Solar Cells. 2017;169:215-21.
[10] Xu T, Li Y, Chen J, Wu H, Zhou X, Zhang Z. Improving thermal management of electronic apparatus with paraffin (PA)/expanded graphite (EG)/graphene (GN) composite material. Applied Thermal Engineering. 2018;140:13-22.
[11] Saffari M, de Gracia A, Ushak S, Cabeza LF. Passive cooling of buildings with phase change materials using whole-building energy simulation tools: A review. Renewable and Sustainable Energy Reviews. 2017;80:1239-55.
[12] Solé A, Falcoz Q, Cabeza LF, Neveu P. Geometry optimization of a heat storage system for concentrated solar power plants (CSP). Renewable Energy. 2018;123:227-35.
[13] Ruiz-Cabañas FJ, Jové A, Prieto C, Madina V, Fernández AI, Cabeza LF. Materials selection of steam-phase change material (PCM) heat exchanger for thermal energy storage systems in direct steam generation facilities. Solar Energy Materials and Solar Cells. 2017;159:526-35.

[14] Vigneswaran VS, Kumaresan G, Dinakar BV, Kamal KK, Velraj R. Augmenting the productivity of solar still using multiple PCMs as heat energy storage. Journal of Energy Storage. 2019;26.

[15] Karimi G, Azizi M, Babapoor A. Experimental study of a cylindrical lithium ion battery thermal management using phase change material composites. Journal of Energy Storage. 2016;8:168-74.

[16] Korti AIN, Tlemsani FZ. Experimental investigation of latent heat storage in a coil in PCM storage unit. Journal of Energy Storage. 2016;5:177-86.

[17] Al Siyabi I, Khanna S, Mallick T, Sundaram S. An experimental and numerical study on the effect of inclination angle of phase change materials thermal energy storage system. Journal of Energy Storage. 2019;23:57-68.

[18] Hasan A, Sarwar J, Alnoman H, Abdelbaqi S. Yearly energy performance of a photovoltaic-phase change material (PV-PCM) system in hot climate. Solar Energy. 2017;146:417-29.

[19] Senthil R, Cheralathan M. Enhancement of the thermal energy storage capacity of a parabolic dish concentrated solar receiver using phase change materials. Journal of Energy Storage. 2019;25.

[20] Maatallah T, Zachariah R, Al-Amri FG. Exergo-economic analysis of a serpentine flow type water based photovoltaic thermal system with phase change material (PVT-PCM/water). Solar Energy. 2019;193:195-204.

[21] Chaiyat N. Energy and economic analysis of a building air-conditioner with a phase change material (PCM). Energy Conversion and Management. 2015;94:150-8.

[22] Arıcı M, Bilgin F, Nižetić S, Karabay H. PCM integrated to external building walls: An optimization study on maximum activation of latent heat. Applied Thermal Engineering. 2020;165.

[23] Pereira R, Aelenei L. Optimization assessment of the energy performance of a BIPV/T-PCM system using Genetic Algorithms. Renewable Energy. 2019;137:157-66.

[24] Haillot D, Franquet E, Gibout S, Bédécarrats J-P. Optimization of solar DHW system including PCM media. Applied Energy. 2013;109:470-5.

[25] Du Y, Mak CM, Li Y. Application of a multi-variable optimization method to determine

lift-up design for optimum wind comfort. Building and Environment. 2018;131:242-54.

[26] Du Y, Mak CM, Li Y. A multi-stage optimization of pedestrian level wind environment and thermal comfort with lift-up design in ideal urban canyons. Sustainable Cities and Society. 2019;46.

[27] Starke AR, Cardemil JM, Colle S. Multi-objective optimization of a solar-assisted heat pump for swimming pool heating using genetic algorithm. Applied Thermal Engineering. 2018;142:118-26.

[28] Ahmadi-Nezamabad H, Zand M, Alizadeh A, Vosoogh M, Nojavan S. Multi-objective optimization based robust scheduling of electric vehicles aggregator. Sustainable Cities and Society. 2019;47.

[29] Shakouri G H, Rahmani M, Hosseinzadeh M, Kazemi A. Multi-objective optimization-simulation model to improve the buildings' design specification in different climate zones of Iran. Sustainable Cities and Society. 2018;40:394-415.

[30] Tavakoli Ghazi Jahani MA, Nazarian P, Safari A, Haghifam MR. Multi-objective optimization model for optimal reconfiguration of distribution networks with demand response services. Sustainable Cities and Society. 2019;47.

[31] Ozcan-Deniz G, Zhu Y. Multi-objective optimization of greenhouse gas emissions in highway construction projects. Sustainable Cities and Society. 2017;28:162-71.

[32] Yang R, Wang L. Multi-objective optimization for decision-making of energy and comfort management in building automation and control. Sustainable Cities and Society. 2012;2:1-7.

[33] Dorotić H, Pukšec T, Duić N. Multi-objective optimization of district heating and cooling systems for a one-year time horizon. Energy. 2019;169:319-28.

[34] Bellos E, Tzivanidis C. Multi-objective optimization of a solar driven trigeneration system. Energy. 2018;149:47-62.

[35] Rey A, Zmeureanu R. Multi-objective optimization framework for the selection of configuration and equipment sizing of solar thermal combisystems. Energy. 2018;145:182-94.

[36] Movahediyan Z, Askarzadeh A. Multi-objective optimization framework of a photovoltaic-diesel generator hybrid energy system considering operating reserve.

Sustainable Cities and Society. 2018;41:1-12.

[37] Bezerra MA, Santelli RE, Oliveira EP, Villar LS, Escaleira LA. Response surface methodology (RSM) as a tool for optimization in analytical chemistry. Talanta. 2008;76:965-77.

[38] Deb K, Pratap A, Agarwal S, Meyarivan T. A fast and elitist multiobjective genetic algorithm: NSGA-II. IEEE transactions on evolutionary computation. 2002;6:182-97.

[39] Hwang C-L, Masud ASM. Multiple objective decision making—methods and applications: a state-of-the-art survey: Springer Science & Business Media; 2012.

[40] Yadav Y, Tiwari G. Analytical model of solar swimming pool: transient approach. Energy conversion and management. 1987;27:49-54.

[41] Dang A. A parametric study of swimming pool heating—I. Energy Conversion and management. 1986;26:27-31.

[42] Katsaprakakis DA. Comparison of swimming pools alternative passive and active heating systems based on renewable energy sources in Southern Europe. Energy. 2015;81:738-53.

[43] Chan WW, Lam JC. Energy-saving Supporting Tourism Sustainability: A Case Study of Hotel Swimming Pool Heat Pump. Journal of Sustainable Tourism. 2003;11:74-83.

[44] Lam JC, Chan WW. Life cycle energy cost analysis of heat pump application for hotel swimming pools. Energy Conversion and Management. 2001;42:1299-306.

[45] Kelly NJ, Tuohy PG, Hawkes AD. Performance assessment of tariff-based air source heat pump load shifting in a UK detached dwelling featuring phase change-enhanced buffering. Applied Thermal Engineering. 2014;71:809-20.

[46] Li Y, Huang G, Wu H, Xu T. Feasibility study of a PCM storage tank integrated heating system for outdoor swimming pools during the winter season. Applied Thermal Engineering. 2018;134:490-500.

[47] Li Y, Huang G, Xu T, Liu X, Wu H. Optimal design of PCM thermal storage tank and its application for winter available open-air swimming pool. Applied Energy. 2018;209:224-35.

[48] Han H-Z, Li B-X, Wu H, Shao W. Multi-objective shape optimization of double pipe heat exchanger with inner corrugated tube using RSM method. International Journal of

Thermal Sciences. 2015;90:173-86.

[49] Flick S, Schwager M, McCarthy E, Mérida W. Designed experiments to characterize PEMFC material properties and performance. Applied Energy. 2014;129:135-46.

[50] Su L, Zhang J, Wang C, Zhang Y, Li Z, Song Y, et al. Identifying main factors of capacity fading in lithium ion cells using orthogonal design of experiments. Applied Energy. 2016;163:201-10.

[51] Shirazi A, Taylor RA, Morrison GL, White SD. A comprehensive, multi-objective optimization of solar-powered absorption chiller systems for air-conditioning applications. Energy Conversion and Management. 2017;132:281-306.

[52] Eini S, Shahhosseini H, Delgarm N, Lee M, Bahadori A. Multi-objective optimization of a cascade refrigeration system: Exergetic, economic, environmental, and inherent safety analysis. Applied Thermal Engineering. 2016;107:804-17.

[53] Jia Z, Ierapetritou MG. Generate Pareto optimal solutions of scheduling problems using normal boundary intersection technique. Computers & Chemical Engineering. 2007;31:268-80.

[54] Bre F, Fachinotti VD. A computational multi-objective optimization method to improve energy efficiency and thermal comfort in dwellings. Energy and Buildings. 2017;154:283-94.

[55] Sayyaadi H, Mehrabipour R. Efficiency enhancement of a gas turbine cycle using an optimized tubular recuperative heat exchanger. Energy. 2012;38:362-75.

[56] Srinivasan V, Shocker AD. Linear programming techniques for multidimensional analysis of preferences. Psychometrika. 1973;38:337-69.

[57] Etghani MM, Shojaeefard MH, Khalkhali A, Akbari M. A hybrid method of modified NSGA-II and TOPSIS to optimize performance and emissions of a diesel engine using biodiesel. Applied Thermal Engineering. 2013;59:309-15.

[58] Wan H, Xu X, Li A, Yan T, Gang W. A wet-bulb temperature-based control method for controlling the heat balance of the ground soil of a hybrid ground-source heat pump system. Advances in Mechanical Engineering. 2017;9.

[59] CLP tariff structure, available at https://www.clp.com.hk/en/customer-service/tariff/business-and-other-customers/bulk-tariff, in.

[60] Buonomano A, De Luca G, Figaj RD, Vanoli L. Dynamic simulation and thermo-

economic analysis of a PhotoVoltaic/Thermal collector heating system for an indoor–outdoor swimming pool. Energy Conversion and Management. 2015;99:176-92.

[61] Somwanshi A, Tiwari AK, Sodha MS. Feasibility of earth heat storage for all weather conditioning of open swimming pool water. Energy Conversion and Management. 2013;68:89-95.

[62] Smith C, Jones R, Lof G. Energy requirements and potential savings for heated indoor swimming pools. ASHRAE Transactions-American Society of Heating Refrigerating Airconditioning Engin. 1993;99:864-76.

[63] Ruiz E, Martínez PJ. Analysis of an open-air swimming pool solar heating system by using an experimentally validated TRNSYS model. Solar Energy. 2010;84:116-23.

[64] Bergman TL, Incropera FP. Fundamentals of heat and mass transfer: John Wiley & Sons; 2011.

[65] Wu S, Fang G. Dynamic performances of solar heat storage system with packed bed using myristic acid as phase change material. Energy and Buildings. 2011;43:1091-6.

[66] Pereira da Cunha J, Eames P. Thermal energy storage for low and medium temperature applications using phase change materials – A review. Applied Energy. 2016;177:227-38.

[67] Watanabe T, Kikuchi H, Kanzawa A. Enhancement of charging and discharging rates in a latent heat storage system by use of PCM with different melting temperatures. Heat Recovery Systems and CHP. 1993;13:57-66.

Appendix A

The schematic for the simulation platform of the system in TRNSYS is presented in Fig. A1. The system comprises a PID controller, a global controller, a PST, two heat exchangers with the effectiveness of 0.95, six pumps, three AHPs, an OSP, two mixing valves, and two diverting valves.

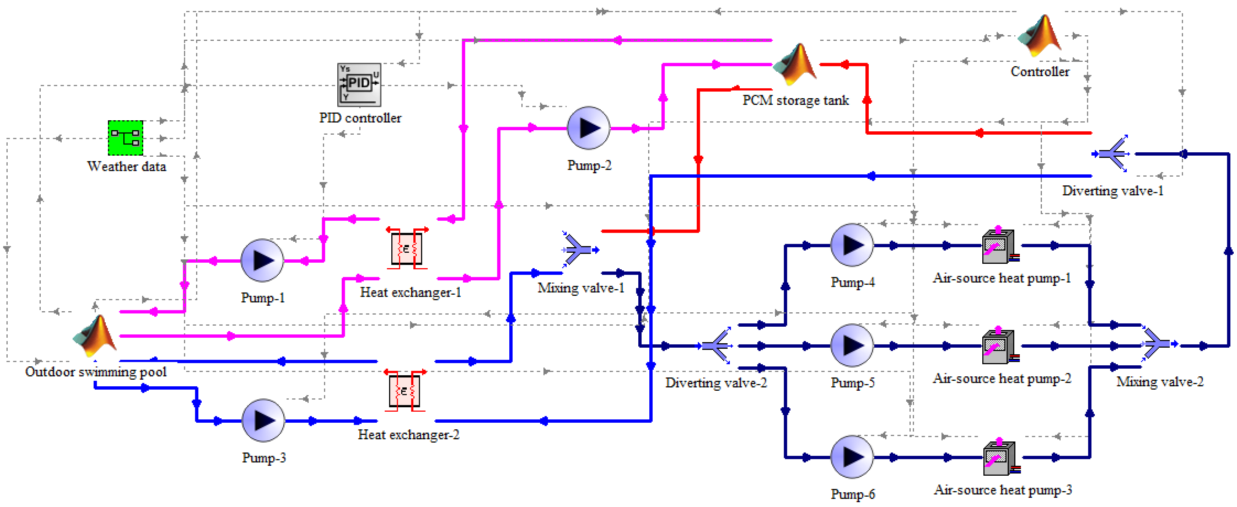

Fig. A1. Schematic for the simulation platform of the system in TRNSYS.

Appendix B

Experimental parameters in the study of Ruiz et al. [63] and Watanabe et al. [67] were presented in Table B1 and B2.

Table B1 Experimental parameters in the study of Ruiz et al. [63]

Parameters	Values
Water surface area of OSP	$50m^2$
Volume of OSP	$82.5m^3$
City	Alicante
Country	Spain

Table B2 Experimental parameters in the study of Watanabe et al. [67]

Parameters	Values
Number of tubes	105
Length of tank	414mm
Wide of tank	198mm
Deep of tank	150mm

Comparison between experimental and simulated results of the OSP model was presented in

Fig. B1. Comparison between the experimental and simulated results of the PST model: (a) charging and (b) discharging process were presented in Fig. B2.

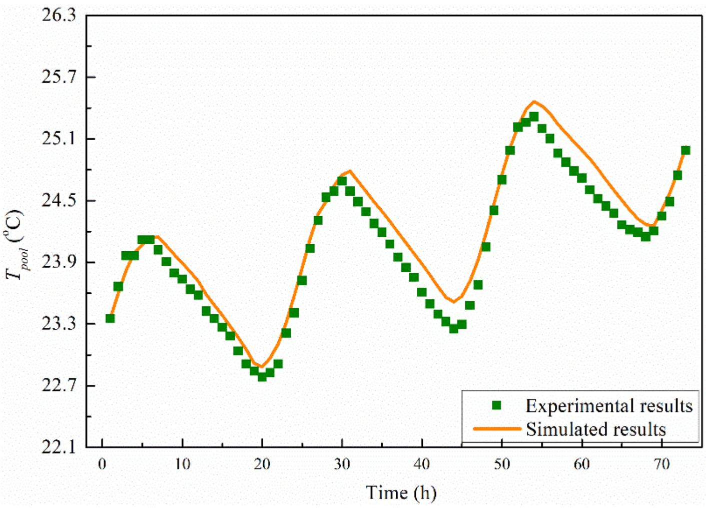

Fig. B1. Comparison between experimental and simulated results of the OSP model.

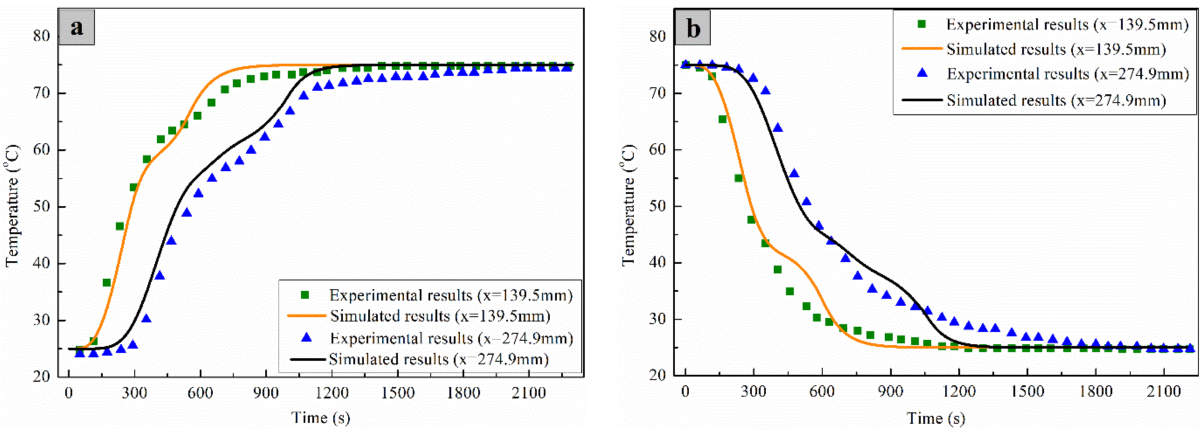

Fig. B2. Comparison between the experimental and simulated results of the PST model: (a) charging and (b) discharging process.

Appendix C

Fig. C1 presents the Pareto optimal solutions and final optimal solutions identified by FDM methods for double-objective optimization of minimizing total energy use (e_t) and initial cost (c_{it}). The design constraint was that the thermal comfort unmet time percentage (t_{cp}) should be less than 2%. It was observed that the value of e_t was 2,276.9MWh when the value of c_{it}

was \$152,254; and the value of e_t was 2,227.0MWh when the value of c_{it} was \$164,450. In the LINMAP and TOPSIS approaches, the ideal and non-ideal solution were respectively the solution that the value of e_t was 2,227.0MWh and the value of c_{it} was \$152,254, and the solution that the value of e_t was 2,276.9MWh and the value of c_{it} was \$164,450. The LINMAP solution was the solution that the value of e_t was 2,262.4MWh and the value of c_{it} was \$153,431. The TOPSIS solution was the solution that the value of e_t was 2,264.8MWh and the value of c_{it} was \$153,111.

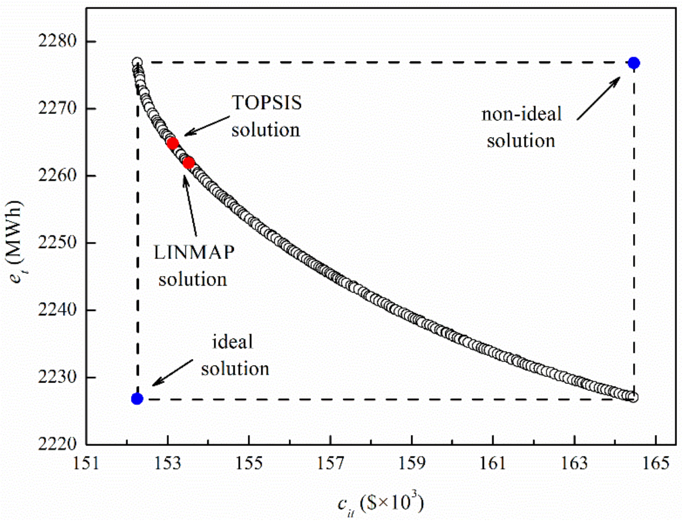

Fig. C1. Pareto and final optimal solutions identified by FDM methods for double-objective optimization: variations of e_t with c_{it}.

Appendix D

Detailed results including volume of PST (V_p), heating capacity of AHPs (q_a), initial cost of AHPs (c_{iap}), initial cost of PST (c_{ipt}), thermal comfort unmet time percentage (t_{cp}), total energy use (e_t), and lifecycle expense (c_l) in different representative Pareto solutions were presented. Table D1, D2, and D3 presents the detailed results of the optimization for minimizing e_t and t_{cp}, minimizing c_l and t_{cp}, and minimizing e_t and c_l, respectively. It should be noted that the initial cost of thermal-insulation cover, pumps, controllers, and heat exchangers were constant since their quantity were constant. The c_{itc}, c_{ip}, c_{icr}, and c_{ihe} were \$4,576, \$3,978, \$6,663, and \$1,560, respectively.

Table D1 Detailed results of the optimization for minimizing e_t and t_{cp}

Representative solutions	V_p (m^3)	q_a (kW)	c_{iap} (\$)	c_{ipt} (\$)	t_{cp} (%)	e_t (MWh)	c_l (\$)
$t_{cp} = 1.02\%$	102.6	219.8	108,530	32,377	1.02	2,356.8	379,300
$t_{cp} = 3.01\%$	95.3	178.0	87,895	30,067	3.01	2,075.1	329,342
$t_{cp} = 4.97\%$	79.7	143.8	70,985	25,157	4.97	1,771.0	284,709
$t_{cp} = 7.02\%$	42.1	93.0	45,894	13,284	7.02	1,153.7	206,724

Table D2 Detailed results of the optimization for minimizing c_l and t_{cp}

Representative solutions	V_p (m^3)	q_a (kW)	c_{iap} (\$)	c_{ipt} (\$)	t_{cp} (%)	e_t (MWh)	c_l (\$)
$t_{cp} = 0.99\%$	130.9	206.6	102,015	41,314	0.99	2,064.4	388,770
$t_{cp} = 3.00\%$	74.9	181.2	89,463	23,617	3.00	1,958.5	338,776
$t_{cp} = 4.99\%$	25.1	147.2	72,658	7,906	4.99	1,480.3	286,219
$t_{cp} = 7.00\%$	15.3	89.5	44,188	4,827	7.00	1,008.7	200,914

Table D3 Detailed results of the optimization for minimizing e_t and c_l

Representative solutions	V_p (m^3)	q_a (kW)	c_{iap} (\$)	c_{ipt} (\$)	t_{cp} (%)	e_t (MWh)	c_l (\$)
$c_l = \$379,993$	49.2	243.8	120,364	15,536	2.00	2,269.0	379,993
$c_l = \$383,036$	36.3	256.4	126,617	11,444	2.00	2,254.5	383,036
$c_l = \$385,994$	28.7	265.8	131,236	9,070	2.00	2,245.1	385,994
$c_l = \$389,030$	23.0	274.2	135,388	7,243	2.00	2,237.8	389,030

Appendix E

The formula for identifying the maximum volume of PST (V_{mp}) is shown as the following equation:

$$V_{mp} = \frac{E_{st}}{c_{lp}\rho_{pcm}(1-\varepsilon_{wt})(T_{pt}-T_{pm}) + H_{pm}\rho_{pcm}(1-\varepsilon_{wt}) + c_{sp}\rho_{pcm}(1-\varepsilon_{wt})(T_{pm}-T_{dpl}) + c_{wt}\rho_{wt}\varepsilon_{wt}(T_{pt}-T_{dpl})} \quad \text{(E1)}$$

where E_{st} is the maximum required thermal energy of the OSP during the open period for satisfying thermal comfort requirements; c_{lp} is the liquid specific heat of PCM; c_{sp} is the solid specific heat of PCM; T_{pt} is the designed maximum temperature that AHPs can heat up to; T_{pm} is the melting temperature of PCM; H_{pm} is the latent heat of PCM; and ρ_{pcm} is the density of PCM.